

Core–shell structured magnesia–silica as a next generation catalyst for one-step ethanol-to-butadiene Lebedev process



Sang-Ho Chung^{a,*¹}, Juan Carlos Navarro de Miguel^{a¹}, Teng Li^a, Polina Lavrik^a, Sarah Komaty^a, Youyou Yuan^b, Daria Poloneeva^a, Wejdan H. Anbari^a, Mohamed Nejib Hedhili^b, Moussa Zaarour^a, Cristina Martín^a, Tuiana Shoinkhorova^a, Edy Abou-Hamad^b, Jorge Gascon^a, Javier Ruiz-Martínez^{a,*}

^a King Abdullah University of Science and Technology, KAUST Catalysis Center (KCC), Thuwal 23955, Saudi Arabia

^b King Abdullah University of Science and Technology, Core Labs, Thuwal 23955, Saudi Arabia

ARTICLE INFO

Keywords:

Ethanol
Butadiene
Lebedev process
Magnesium silicate
Core–shell catalyst

ABSTRACT

Over 70 years, silica–magnesia catalyst prepared by wet-kneading method has been a benchmark for one-step ethanol-to-butadiene Lebedev process. Recent studies showed that wet-kneading provides an environment for the concomitant dissolution and cross-deposition of silicon and magnesium subunits, which can lead to the formation of not only the beneficial sites (Si on MgO), but also the detrimental ones (Mg on SiO₂) for the Lebedev process. The use of conventional silica sources to formulate the silica–magnesia catalysts should be revisited, as they will be eventually dissolved and redispersed on MgO and the remaining SiO₂ particles would be used for the formation of detrimental sites. In this regard, we demonstrated core–shell structured MgO–SiO₂ catalysts as a second generation of Lebedev catalyst, where the Si subunits were selectively deposited on the MgO nanoparticles as surface magnesium silicates. Compared to the conventional wet-kneaded silica–magnesia catalyst system, we could reduce the amount of Si source by ~40 times with the enhanced catalytic performance towards butadiene.

1. Introduction

1,3-Butadiene (butadiene) finds its various applications in polymer industry such as styrene-butadiene rubber (SBR), acrylonitrile-butadiene-styrene rubber (ABS) and poly-butadiene-styrene rubber (PBR) [1–3]. Currently, over 95% of butadiene is produced as a byproduct from ethylene production units, that is, in naphtha steam crackers. The recent unstable oil prices and the issues related to the environment and climate changes have urged to find an alternative process for butadiene production [4–7]. Taken together with recent availability of bioethanol, ethanol-to-butadiene process is considered as a sustainable alternative [1,6,8,9]. Compared to two-step ethanol-to-butadiene process (Ostromislensky process [10]), where ethanol is partially converted to acetaldehyde by dehydrogenation first and then the mixture of ethanol and acetaldehyde is reacted to form butadiene [11], one-step Lebedev process has its advantages of the greater process simplicity with economic perspectives [4].

The most plausible mechanism for the one-step ethanol-to-butadiene process involves ethanol dehydrogenation to acetaldehyde as a first step [8,12–15]. Then, multiple reactions such as aldol condensation between two acetaldehydes to form 3-hydroxybutanal (acetaldol), subsequent dehydration to crotonaldehyde and hydrogenation step to crotal alcohol by Meerwein–Ponndorf–Verley reduction, and the intramolecular dehydration eventually occur to yield butadiene [5,8,12–16]. Owing to these multiple steps, multi-functional catalysts are typically required for ethanol-to-butadiene process, especially having both acidic and basic sites [12,17–24].

In particular, silica–magnesia has been a benchmark catalyst over 70 years, considering its originality in the industrial process and its stable catalytic performance [25]. The catalytic performance of the silica–magnesia catalyst is largely influenced by preparation procedures, and wet-kneading method can generate the most active silica–magnesia catalyst [3,17]. Wet-kneading typically utilizes solid precursors such as Stöber silica and magnesium hydroxide in water under continuous

* Corresponding authors.

E-mail addresses: sangho.chung@kaust.edu.sa (S. Chung), javier.ruizmartinez@kaust.edu.sa (J. Ruiz–Martínez).

¹ These authors (S.-H. Chung and J.C. Navarro de Miguel) contributed equally.

mixing (Fig. 1a) [20]. As the pristine MgO and SiO₂, and their physical mixtures show limited catalytic performances, the magnesium silicates (Mg–O–Si) formed during wet-kneading have been considered as active sites for one-step Lebedev process (Fig. 1a) [17–20,22,26]. In recent years, the formation of different magnesium silicates have been evidenced [3,17–20,22,26,27], which is originated by the dissolution and cross-deposition of Si and Mg subunits during the wet-kneading [20,28]. Several magnesium silicate phases can be formed as a result of the dissolution and cross-deposition, and the magnesium silicates can show their distinct structures and catalytic performances in the Lebedev process. More specifically, two distinct phases (Si on MgO and Mg on SiO₂) can be formed during the conventional wet-kneading. The two phases can be separated via modified wet-kneading, and it was reported that the phases exhibit different catalytic activity, that is, the production of butadiene and ethylene, respectively. Meanwhile, the Mg/SiO₂ is responsible for the formation of ethylene, which does not go to the direction of ethanol-to-butadiene pathway, due to its high acidic properties. The two phases can be separated via modified wet-kneading, which can lead to the preferential formation of butadiene and ethylene, respectively [28].

In this regard, the expenses of conventional silica sources to formulate the active silica–magnesia catalysts can be revisited, since they will be dissolved and redispersed on MgO (Si on MgO) and the remaining SiO₂ particles would be used for the formation of detrimental acid sites (Mg on SiO₂). In this study, to fully utilize Si to form active sites selective to butadiene (Si subunits on the surface of MgO), we report a series of core-shell structured MgO–SiO₂ catalysts with different amount of Si for one-step ethanol-to-butadiene Lebedev process (Fig. 1b). Compared to the conventional wet-kneaded silica–magnesia catalyst system, we could reduce the amount of Si source by ~40 times, while showing enhanced catalytic activity towards butadiene.

2. Experimental section

2.1. Catalyst synthesis

Firstly, magnesium hydroxide (Mg(OH)₂) as core material was obtained via precipitation [20,22,28], adding a 0.4 M sodium hydroxide

solution (Sigma-Aldrich) dropwise to a 0.2 M aqueous magnesium nitrate solution (Fluka). After the pH 12 is reached, the solution was aged for 1 h with constant stirring. The precipitated Mg(OH)₂ platelets were separated by centrifugation and washed thoroughly with deionized water and dried overnight in a convection oven at 120 °C. The core–shell structured MgO–SiO₂ catalysts were prepared from the Mg(OH)₂ and tetraethyl orthosilicate (TEOS, Aldrich) after modification to the previously reported procedure using cetyltrimethylammonium bromide (CTAB) [29]. The Mg(OH)₂ containing solution was prepared by adding Mg(OH)₂ to a solution of anhydrous ethanol (VWR Chemicals), deionized water (18.2 MΩ), and an ammonium hydroxide solution (25%, Alfa Aesar). After adding CTAB (Affymetrix) to the solution, the mixture was stirred for 30 min to obtain clear and homogeneous solution. For homogeneous core–shell structure, the desired amount of TEOS was diluted in ethanol solution and added dropwise to the Mg(OH)₂ containing solution with continuous stirring. After 24 h, solid particles were separated by centrifugation and washed multiple times with deionized water. The as-made solid samples were dried overnight in a convection oven at 120 °C. The traces of sodium in the samples was analyzed by inductive coupled plasma optical emission spectroscopy (ICP-OES). For the pristine Mg(OH)₂ and the core–shell structured MgO–SiO₂ catalysts, 0.24 and 0.04 (± 0.01) wt% of sodium were observed, respectively, suggesting that the occluded sodium in the pristine Mg(OH)₂ was further dissolved away during the sequential core–shell synthesis method. The samples were finally calcined at 500 °C for 5 h with a heating ramp of 5 °C min⁻¹. The calcined catalysts are denoted with Si/Mg ratio as cs-Si/Mg-ratio. The pristine MgO was obtained by calcination of Mg(OH)₂ and the pristine SiO₂ was precipitated based on the above procedure without Mg(OH)₂ as core-material. For comparison, the conventional wet-kneaded SiO₂–MgO catalyst was prepared with 4 h of wet-kneading time [17,20,22,28].

2.2. Characterization

Thermal gravimetric analysis coupled with mass spectrometry (TGA–MS) was performed using a Mettler Toledo TGA/DSC1 Star^e System under airflow. The sample mass is typically ~15 mg and the heating program was set as same as the calcination step under

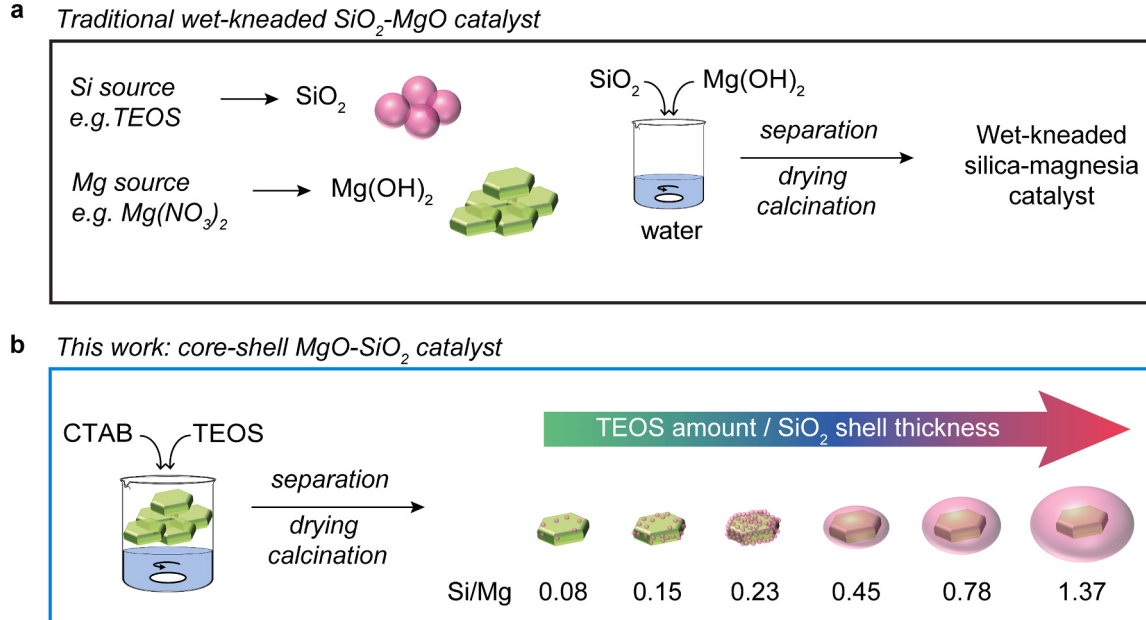


Fig. 1. Schematic of the synthetic process for one-step ethanol-to-butadiene catalysts. Illustrations of the preparation for (a) the conventional wet-kneaded silica–magnesia catalysts and (b) the core–shell structured MgO–SiO₂ catalyst, from platelet shaped magnesium hydroxide (Mg(OH)₂) as core material in this study. The Si/Mg ratio has been obtained from ICP-OES results. Abbreviations: CTAB (cetyltrimethylammonium bromide), TEOS (tetraethyl orthosilicate).

continuous air flow of 20 mL min⁻¹.

Scanning electron microscopy (SEM) analysis was carried out with Zeiss Merlin with in-lens detector. The samples were coated with a 2 nm layer of platinum (Pt) prior to SEM imaging. The operation conditions were 3 kV and 70 pA. For the focused ion beam SEM, the sample was coated with 15 nm layer of Pt in a sputter coater prior loading it into microscope. Dual Beam Helios G4 UX SEM-FIB was used to deposit an additional 1 μm layer of Pt to protect region of interest before cutting it with Ga ions. Later, the cut was imaged using Zeiss Merlin with in-lens detector.

High-angle annular dark-field scanning transmission electron microscopy (HAADF-STEM) and electron energy loss spectroscopy (EELS) measurements were performed using a double aberration-corrected Titan Themis Z (Thermo Fisher Scientific) microscope operated at 300 kV. EELS mappings were obtained using an electron counting detector Gatan K3 installed in a Gatan Continuum GIF. To create maps, 256 × 256 probe positions were used with a 0.6–0.9 nm step size, a dwell time of 5 ms, and a beam current of 70 pA. Transmission electron microscopy (TEM) micrographs were acquired using a Titan ST microscope operated at an acceleration voltage of 300 kV and with a 0.5–0.8 nA beam current.

Elemental analysis for Na, Si and Mg was conducted by ICP-OES on an Agilent 5100 ICP-OES instrument using argon as the carrier gas. The digestion of the samples was executed with a solution containing a mixture of hydrochloric acid, nitric acid and hydrofluoric acid (6:2:1 v/v ratio) at max settings of 273 °C and 35 bar on an UltraWAVE apparatus (Milestone).

Powder X-ray diffraction (PXRD) patterns were acquired on a Bruker D8 Advance operated at 40 kV and 40 mA using monochromatic Cu K α ($\lambda = 1.5406 \text{ \AA}$) radiation, while applying a scan speed of 8 s step⁻¹ and a step size of 0.03° over a 2θ range of 5–80°. Crystalline phase identifications were conducted in Diffract.Eva software with the help of the PDF-4 + (2019) crystal database. For the pair distribution function analysis, the raw data was collected on D8 discover system with a Focuseed Gobbel Mirror and 2D eiger detector in a 0.5 mm capillary. The X-ray source was molybdenum with a wavelength of 0.703 Å. The raw data were reduced with PDFgetX3 to get the PDF data g(r) and the PDF data was refined with a small box model with TOPAS 6 PDF refinement module. The empty capillary pattern was also collected as the background.

Nitrogen (N₂) physisorption was measured at -196 °C using a Micromeritics ASAP 2420 high-throughput analysis system. Samples were outgassed at 300 °C under vacuum for 8 h. The specific surface areas were estimated according to the Brunauer–Emmett–Teller (BET) method. Pore size distribution (PSD) was calculated using the classic nonlocal density functional theory (NLDFT) method combined with isotherms at -196 °C cylindrical model by SAIEUS (Solution of Adsorption Integral Equation Using Splines-Micromeritics) software. For the data fitting, values for lambda were set between 2.5 and 3 and standard deviations of the fits was between 0.75 and 0.98.

X-ray photoelectron spectroscopy (XPS) studies were carried out in a Kratos Axis Ultra DLD spectrometer equipped with a monochromatic Al K α X-ray source ($h\nu = 1486.6 \text{ eV}$) operating at 75 W, a multi-channel plate and delay line detector under a vacuum of ~10⁻⁹ mbar. All spectra were recorded using an aperture slot of 300 μm × 700 μm. Survey spectra were collected using a pass energy of 160 eV and a step size of 1 eV. A pass energy of 20 eV and a step size of 0.1 eV were used for the high-resolution spectra. For XPS analysis samples were mounted in floating mode to avoid differential charging. The charge neutralization was required for all samples. Binding energies were referenced to the C 1s binding energy of adventitious carbon contamination which was taken to be 284.8 eV.

The 1D ¹H-²⁹Si CP spectrum was recorded on a Bruker 900 MHz with 3.2 mm HXY probe, using a 4 s recycle delay, 33 ms acquisition time, and 17408 scans with the MAS frequency of 20 kHz. During the CP step, ¹H CP spin-lock pulses centered at 38 kHz were linearly ramped from 75

to 100% and the ²⁹Si RF field was matched to obtain an optimal signal. The ²⁹Si chemical shifts were referenced externally to hexamethyl cyclosiloxane.

Temperature programmed desorption of ammonia (NH₃-TPD) was performed in the Micro-activity Reference setup (PID Eng&Tech). 100 mg of catalyst were placed in a fixed bed quartz tube reactor. The concentrations of inlet and outlet of NH₃ were recorded by MultiGasTM 2030 FT-IR continuous gas analyzer. The sample was pretreated under N₂ at 350 °C for 30 min (ramp rate 10 °C min⁻¹). After cooling down to 40 °C, the sample was exposed to 10 mL min⁻¹ of NH₃ flow for 40 min (3% NH₃ balanced in N₂). The physisorbed NH₃ was removed by purging with 100 mL min⁻¹ of N₂ flow for 60 min. Finally, the desorption of NH₃ was performed by increasing the temperature from 40 to 600 °C (ramp rate 10 °C min⁻¹). Temperature programmed desorption of carbon dioxide (CO₂-TPD) was performed in the Autochem 2920 system (Micromeritics Instruments Co.). 50 mg of the sample was pretreated at 400 °C for 1 h under helium flow. The sample was cooled down to 100 °C and submitted to CO₂ adsorption for 1 h. The saturated sample was flushed with helium for 1 h to remove physisorbed CO₂, and then the temperature was increased to 700 °C with a heating ramp of 10 °C min⁻¹.

The process simulator Aspen Plus v12 was used for carrying out the calculations, considering the minimization of the Gibbs free energy [7]. Two thermodynamic property packages (NRTL and SRK) are used, but the results obtained were similar. The selectivity for the different products obtained during the ethanol transformation was calculated by Eq. (1).

$$\sigma_{j/\text{EtOH}} = \frac{n_{C,j}}{n_{C,\text{EtOH}}} \cdot \frac{n_j}{n_{\text{EtOH},0}} - \frac{n_{j,0}}{n_{\text{EtOH}}} \quad (1)$$

Where $n_{C,j}$ and $n_{C,\text{EtOH}}$ represent the number of carbon atoms in the product j and ethanol, respectively; n_j and n_{EtOH} are the number of moles of product j and ethanol in the final mixture, respectively; and $n_{j,0}$ and $n_{\text{EtOH},0}$ are the number of moles of product j and ethanol, in the initial mixture.

Diffuse reflectance IR coupled with mass spectroscopy (DRIFTS-MS) study was performed on a Nicolet 6700 FT-IR spectrometer equipped with a liquid nitrogen cooled mercury–cadmium–telluride (MCT) detector combined with an online gas-phase Transpector CPM Mass Spectrometer (1–100 amu). For the temperature programmed surface reaction (TPSR) experiments, ~40 mg of sample was pretreated at 425 °C for 40 min in a He flow (>99.999% purity, 20 mL min⁻¹) with a heating rate of 5 °C min⁻¹. The samples were then cooled to 50 °C and loaded with ethanol for 30 min using He as the carrier gas. After that, the samples were purged with He for 30 min to eliminate the physically adsorbed ethanol at 50 °C. Then, the ethanol TPSR experiment was performed in the range of 50–500 °C (held at 500 °C for 30 min) with a heating rate of 5 °C min⁻¹. For in situ DRIFTS experiments, the same pretreatment procedure was adopted without the cooling step, and ethanol was continuously introduced at 425 °C. The in-situ DRIFT spectra were obtained by subtracting the background of bare catalyst after the pretreatment and the information about the gas-phase ethanol was obtained by flowing ethanol to the cell loaded with KBr. The IR data was processed by means of Kubelka–Munk conversion using OMNIC 8 software (version 8.2.0.387). The online gas phase products were analyzed by MS and referred to the database of the National Institute of Standards and Technology (NIST). The *m/z* values of the reactant and products were referred as follows: hydrogen (2), helium (4), water (17), ethylene (26, 27), ethanol (31), butadiene (39, 54), crotyl alcohol (57), and crotonaldehyde (70). Acetaldehyde is not specified in the MS analysis due to its complexity with other possible products, such as *m/z* = 29 (ethyl radical) and 44 (carbon dioxide). The mass data signal for each *m/z* was processed using a Savitzky–Golay smoothing filter (points of window 10 and polynomial order of 2) in OriginPro 2023 software (version 10.0.0.154).

2.3. Catalytic activity test

The activity tests were carried out in an Avantium four-channel Flowrence XD high-throughput reactor system. The catalytic conversion was evaluated from 325 °C to 500 °C and ambient pressure [22]. The catalyst bed was diluted with silicon carbide in a mass ratio 1:4 (catalyst: SiC) to decrease the effect of axial dispersion and the heat transfer problems along the catalytic bed. Typically, 50 mg catalyst were mixed with 180 mg grit 46 SiC and placed in a quartz tube with an internal diameter of 2.3 mm. the reaction feed composition was set to flow 45 mg h⁻¹ of liquid ethanol in 16 mL min⁻¹ of helium (2.2 vol% of gaseous ethanol in helium and weight hourly space velocity (WHSV) at 0.9 h⁻¹). The unreacted ethanol and reaction products were analyzed by gas chromatography (GC) using an Agilent 7890B gas chromatograph equipped with three detectors (one thermal conductivity detector (TCD) and two flame ionization detectors (FID)). The FID channels were equipped with a 10 m precolumn with a wax stationary phase and a 30 m Gaspro stationary phase to separate ethanol, acetaldehyde, C₁–C₇ hydrocarbons, and oxygenates. The TCD channel contained a PoraPLOT Q GC, a HayeSep Q, and a Molsieve for the analytical column. The product analysis was performed on an Agilent 7890B gas chromatography with Agilent Refinery Gas Analysis (dry basis) and three calibration mixtures with known concentration (Air Liquide) were used to determine the retention time and the response factor for each component, and to calibrate the TCD and FID signals. The response factors for the components (F_i) were calculated based on the following equation:

$$F_i = \frac{A_i}{X_i} \quad (2)$$

where A_i and X_i are the area of the peak and the molar composition corresponding to the component i , respectively. Ethanol conversion (X) and product selectivities (S_i) were calculated using the following formulas:

$$X = \frac{C_{\text{EtOH}_{in}} - C_{\text{EtOH}_{out}}}{C_{\text{EtOH}_{in}}} \times 100 \quad (3)$$

$$S_i = \frac{i \times C_i}{2(C_{\text{EtOH}_{in}} - C_{\text{EtOH}_{out}})} \times 100 \quad (4)$$

where $C_{\text{EtOH},in}$ and $C_{\text{EtOH},out}$ are the concentrations of ethanol in the blank and reactor, respectively, i is the number of carbons in the product i , and C_i is the concentration of product i , determined by GC analysis.

3. Results and discussion

3.1. Catalyst synthesis

Core-shell structured MgO–SiO₂ catalysts were prepared by using platelet-shaped Mg(OH)₂ as a core material, varying the thickness of SiO₂ shell (Si/Mg ratio = 0.08–1.37) (Fig. 1b). To achieve the core–shell structure, we promoted the preferential deposition of Si subunits on the surface of Mg(OH)₂. By using optimized synthesis conditions, CTAB and aqueous ammonia forms micelles in ethanol, and then the hydrolysis of TEOS takes places after diffusion through the micelle walls [29], having silicate monomers and oligomers (SiO₄⁴⁻ species) in the micelles. Then, the deposition of the silicate micelles occurs on the surface of Mg(OH)₂ by electrostatic interaction [20], which results in the formation of the active sites for ethanol-to-butadiene process, that is, magnesium silicates (Mg–O–Si) on the MgO surface after calcination of the material [28]. Meanwhile, for the samples containing higher amount of Si, the TEOS hydrolysis continues at the magnesium silicates surface, which can lead to the growth of SiO₂ shells gradually (Fig. 1b) [29].

Fig. 2 shows the results of thermogravimetric analysis coupled with mass spectrometry (TGA–MS) for the dried core–shell structured Mg(OH)₂–SiO₂ samples. During the analysis, four stages of the sample mass loss were observed (i–iv). The first stage (30–150 °C, stage i) is related to

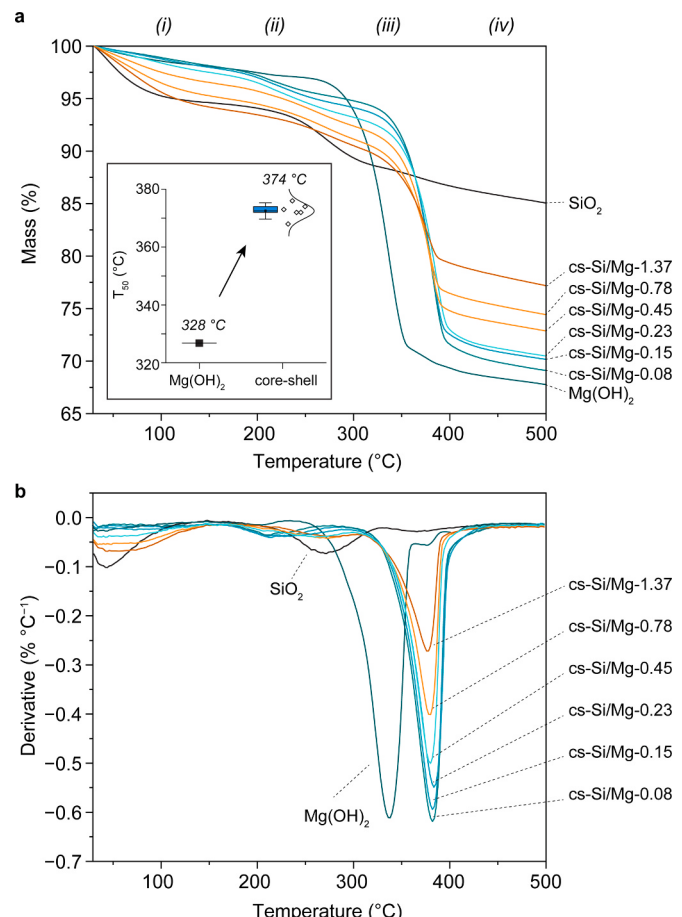


Fig. 2. Thermogravimetric analysis coupled with mass spectrometry (TGA–MS) and for the dried core–shell structured Mg(OH)₂–SiO₂ samples. (a) Thermogravimetric curves and (b) the first-derivatives of the corresponding plots for the samples. The temperature program for TGA–MS is set as same as calcination step, from 30 to 500 °C with the heating ramp of 5 °C/min. In the inset of the figure T_{50} stands for the medium temperature between T_{onset} and T_{offset} for the dehydroxylation of brucite phase to periclase phase. The error of the T_{50} dehydroxylation temperature by TGA was calculated as 2.5 (± 2.1) °C.

the removal of the physisorbed water from the sample surface. The second mass loss between 200 and 350 °C (stage ii) is associated with the decomposition of CTAB, which was evidenced by the online MS identification of fragments from CTAB (CH₃CH₂CH₂ and CO₂, *m/z* 43 and 44) (Fig. S1a) [30]. With the increased amount of Si content of the samples, a higher mass loss was observed, which resulted in a maximum of ~4% of the total mass loss. The decomposition temperature of CTAB shifted to higher temperature for the core–shell structured samples, which is related to the thickness of the porous shell structure (*vide infra*).

During the third step of mass loss (stage (iii)), the dehydroxylation of brucite occurs to form a periclase phase [31,32], which is responsible for ~25% of total mass loss (Fig. 2a). The mass loss at the stage (iii) corresponds to the relative amount of Mg(OH)₂ in the samples. Compared to the pristine Mg(OH)₂, the core–shell structured samples exhibited a dehydroxylation temperature shifted to higher temperatures (~46 °C), due to the formation of surface magnesium silicates (Fig. 2, inset) [28]. For example, in the cs-Si/Mg-0.08 sample, the dehydroxylation occurred at 376 °C ($T_{\text{dehydroxylation}}$ of pristine Mg(OH)₂ = 328 °C). As the dehydroxylation of brucite starts from its surface and then inwards [33], we expect that the incorporation of Si subunit on the surface of Mg(OH)₂ retards the dehydroxylation of surface magnesium species, shifting dehydroxylation to higher temperatures. After brucite dehydroxylation, the fourth step (stage iv) at ~500 °C resulted in the final mass loss of less than 3%, which is related to further surface dehydroxylation.

The calcined core-shell structured MgO–SiO₂ catalysts were imaged by scanning electron microscopy (SEM) and transmission electron microscopy combined with electron energy loss spectroscopy (TEM-EELS) (Fig. 3). The pristine MgO has platelet-shape with the average size of ~50 and ~20 nm for the apothem and the thickness of the platelets, respectively (Fig. 3a,b). The prepared SiO₂ without core-material showed aggregated structures composed of few nanometer-sized particles (<3 nm) (Fig. 3c,d). The SEM and TEM-EELS images of core-shell MgO–SiO₂ structures showed that SiO₂ is selectively deposited on the surface of MgO (Fig. 3e–j, k–v). This suggests that the electrostatic interaction between Si subunits and the surface of Mg(OH)₂ promoted the surface deposition of Si on Mg(OH)₂, while the formation of individual SiO₂ particles is suppressed [20,28]. For example, the low Si content samples (cs-Si/Mg-0.08, 0.15 and 0.23) showed that Si subunits homogeneously decorated MgO surfaces (Fig. 3e–g, k–m). This is in line with the TGA-MS results that the dehydroxylation of the brucite phase was retarded by Si subunits (Fig. 2), due to the formation of magnesium silicates (Mg–O–Si). It should be noted that the formation of magnesium silicates on the surface of MgO created few nanometer sized patterns, which were also observed for the silica-magnesia catalyst prepared by modified wet-kneading (Fig. S2) [28]. For the samples with the higher Si amount, the MgO core-particles were fully coated by a SiO₂ shell with different thicknesses (Fig. 3h–j, t–v). For the cs-Si/Mg-0.45 sample, each MgO particles are covered by a ~10 nm SiO₂ shell (Fig. 3h,n,r). The

further growth of SiO₂ on the surface led to the formation of SiO₂ shell as a continuous domain, as observed for cs-Si/Mg-0.78 and 1.37 catalysts (Fig. 3i,j,o,p). Meanwhile, the dispersion of core MgO materials were still preserved, as confirmed by the cross-sectional image obtained from focused ion beam scanning electron microscopy (FIB-SEM) and TEM-EELS results (Fig. S3, Fig. 3o,p). Fig. 3w represents the average thickness of the SiO₂ shell for the core-shell structured catalysts measured by high-resolution bright-field TEM images (Fig. S4), as a function of the sample Si content.

3.2. Characterization of the core-shell MgO–SiO₂ catalysts

As the textural properties of the core-shell structured catalysts are largely influenced with the shell thickness [34], nitrogen (N₂) physisorption was performed for all the core-shell structured MgO–SiO₂ catalysts (Fig. 4a). The pristine MgO samples exhibited type IV isotherm with the H1 hysteresis, related to the interparticle voids (Fig. S5a). The SiO₂ presented type I isotherms with a sharp N₂ adsorption at the beginning ($p/p_0 \sim 0.04$), indicating the presence of micropores (pore size less than ~2 nm) (Fig. S5) [35,36]. The pore size of the SiO₂ prepared using CTAB is known to be determined by the size and shape of CTAB micelles in the synthesis solution [29,37–40], which are largely dependent on the concentrations of surfactants and solvents [41]. For example, microporous SiO₂ samples can be prepared by CTAB, with the

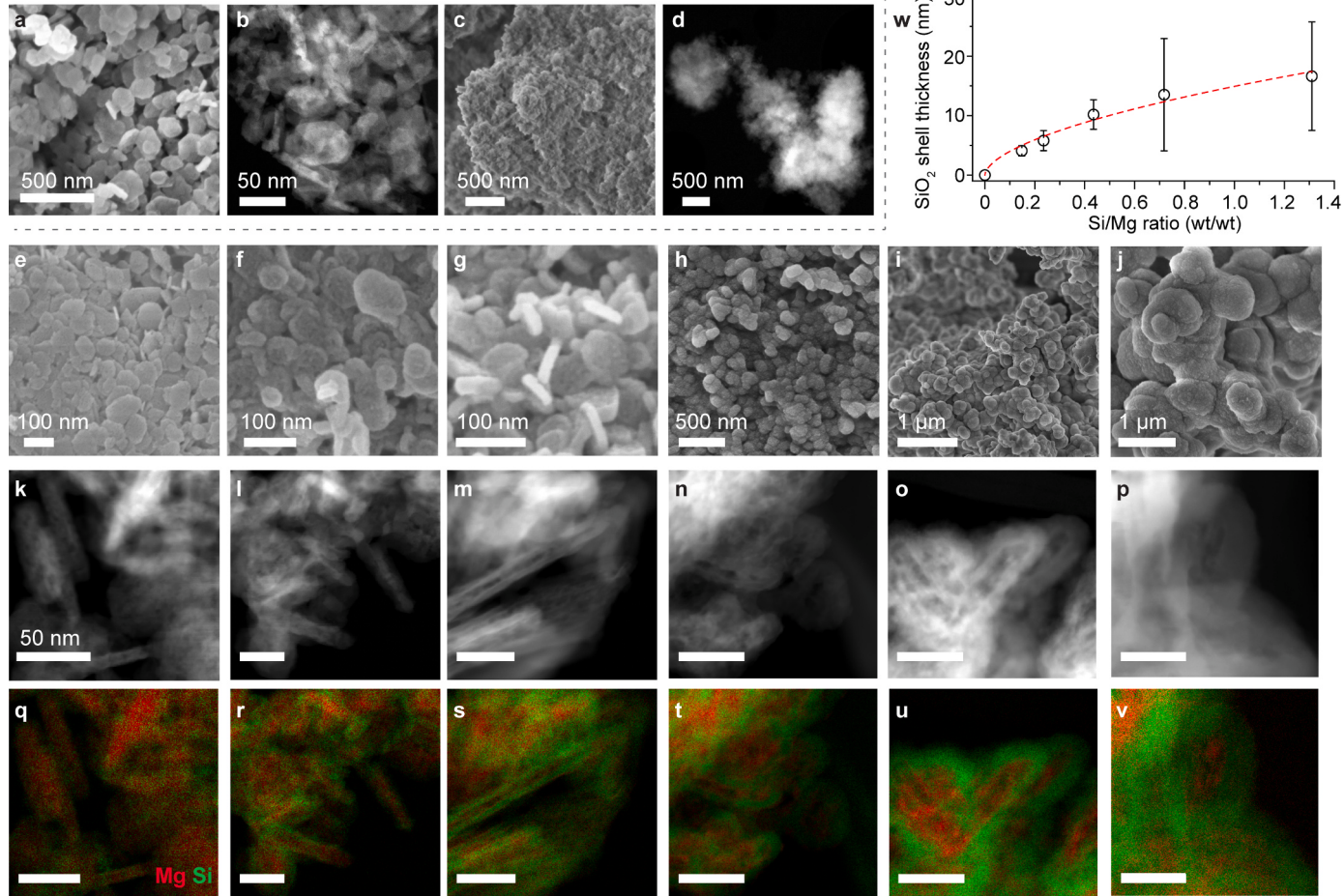


Fig. 3. Electron microscopy images of the calcined core-shell structured MgO–SiO₂ catalysts. Scanning electron microscopy (SEM) images of (a) MgO, (c) SiO₂, (e) cs-Si/Mg-0.08, (f) cs-Si/Mg-0.15, (g) cs-Si/Mg-0.23, (h) cs-Si/Mg-0.45, (i) cs-Si/Mg-0.78, and (j) cs-Si/Mg-1.37. High-angle annular dark-field scanning transmission electron microscopy (HAADF-STEM) images of (b) MgO, (d) SiO₂, (k) cs-Si/Mg-0.08, (l) cs-Si/Mg-0.15, (m) cs-Si/Mg-0.23, (n) cs-Si/Mg-0.45, (o) cs-Si/Mg-0.78, and (p) cs-Si/Mg-1.37. Mg and Si EELS mapping images (q–v) for the core-shell catalysts corresponds to the STEM images (k–p). The scale bar in HAADF-STEM images (k–p) applies to all EELS maps (50 nm). (w) The measured SiO₂ shell thickness over the corresponding ~50 particles from high resolution TEM images (Fig. S4). The data are presented as mean ± s.d. of the measurements. The dotted red line in (w) is added to guide the observed trend.

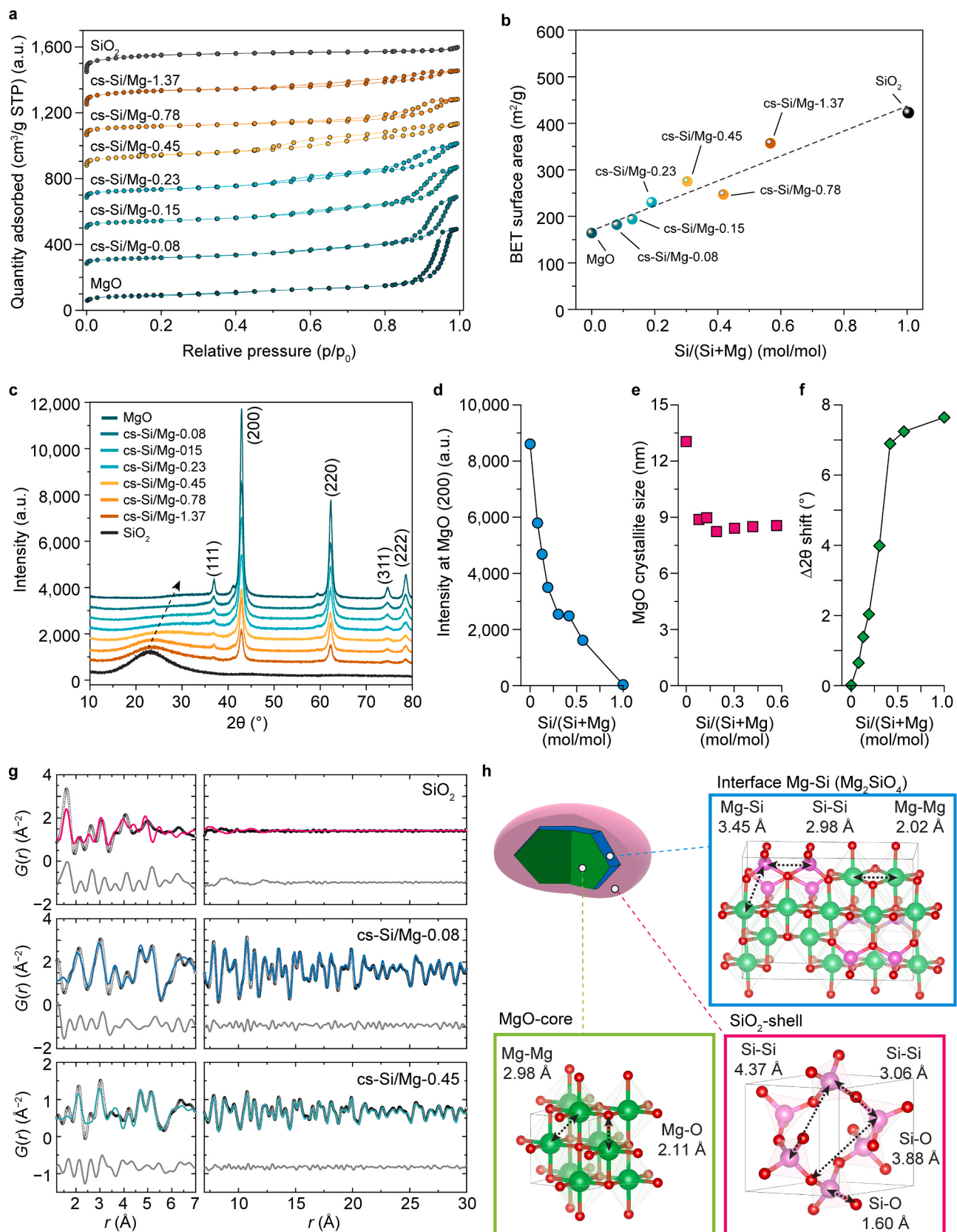


Fig. 4. Nitrogen (N_2) physisorption isotherms (a) and BET surface area as a function of Si content (b) of the calcined core–shell structured $\text{MgO}-\text{SiO}_2$ catalysts. Note that the N_2 isotherms are offset for clarity. The dotted line in (b) is the result of linear fitting of the surface area ($r^2 = 0.93$). (c) Powder X-ray diffraction PXRD patterns of the catalysts. (d) The intensity of MgO (200) plane, (e) MgO crystalline size, and (f) the observed 2θ shifts in the amorphous region (20 – 35°). (g) X-ray pair distribution function (PDF) analysis of the core–shell structured $\text{MgO}-\text{SiO}_2$ catalysts (cs-Si/Mg-0.08 and 0.45) and the pristine SiO_2 . The data were modeled with the referenced structure determined by powder X-ray diffraction. The fitted ranges for with fit ranges of $1 \leq r \leq 10 \text{ \AA}$ (left panels) and $10 \leq r \leq 30 \text{ \AA}$ (right panels). The data are shown as black circles; the fit is the colored line, and the difference is the gray line. (h) Simulated structure based on PDF analysis.

pore size in the range of 1–2 nm [39,40]. At the condition of high CTAB concentration ($C_{CTAB} > CMC$), not only the micelles of CTAB, individual and pre-micellar associates of CTAB molecules can be present in the synthesis solution [41,42]. As the concentration of CTAB (0.018 mol L⁻¹) is ~3 times higher than the CMC based on the regression from Shah et al. (0.006 mol L⁻¹) [42], we expect that the formed micropores on the pristine SiO₂ is resulted from the decomposition of the excess, individual CTAB molecules, which were occluded in the shell-SiO₂ during the synthesis [40].

Meanwhile, the core–shell structures of the catalysts showed hysteresis loops at around p/p_0 0.5, attributed to capillary condensations in mesopores (Fig. S5a), related to the formation of SiO₂-shell on MgO particles. The BET surface area of the prepared catalysts increases linearly with the amount of Si (Fig. 4b).

Figs. S6 and 4c shows the X-ray diffraction (XRD) patterns of the prepared core–shell structured MgO–SiO₂ catalysts. For the dried samples, hexagonal brucite phase (trigonal symmetry, P-3m1) was observed (Fig. S6). After calcination at 500 °C, crystalline periclase phases (cubic symmetry, Fm-3 m) were observed, in line with TGA-MS results (Fig. 2) [56]. The intensities of Mg(OH)₂ (101) and MgO (200) planes decreased for the higher amount of Si in the samples, as expected from their Mg contents in the sample (Fig. 4c,d, Fig. S6). Notably, the crystallite size of periclase phase decreased with the surface decoration of Si subunits (Fig. 4e), which has been also observed for the conventional wet-kneaded SiO₂–MgO catalysts [22,28]. This suggest that, during the dehydroxylation of brucite to periclase phases, the surface Si subunits can regulate the growth of Mg(OH)₂ crystallites, forming magnesium silicates (Mg–O–Si). Few articles reported the PXRD patterns of magnesium silicates phases at 20 33–40° [26,43–45]. We could not observe the related diffractions due to the limited amount of surface magnesium silicates (few layers on MgO), which were only formed at the interface between MgO-core and SiO₂-shell.

Meanwhile, we observed the 2θ shifts of the amorphous silica region (2θ 15–25°) for the calcined catalysts, which were not observed for dried samples (Fig. 4f, Fig. S6). This suggests that the calcination step results in these shifts, that is, the surface dehydroxylation and related formation of magnesium silicates, as observed by TGA-MS analysis (Fig. 2). The local coordination environment and the structure of the core–shell structured MgO–SiO₂ samples were further refined using pair distribution function (PDF) analysis (Fig. 4g,f). For the prepared pristine SiO₂ sample, the bond lengths of 1.62 and 3.06 Å were observed, corresponding to the Si–O and Si–Si, respectively [46,47]. The less intense coherence lengths observed at higher distances (>10 Å) represents the nano-sized and amorphous characteristics of the pristine SiO₂. For cs-Si/Mg-0.08 and 0.45 samples, both the structures of MgO and forsterite (Mg₂SiO₄) with a sphere refinement model were used for the fitting. Compare to the pristine SiO₂ sample, cs-Si/Mg-0.08 did not exhibit the Si–O bond length around 1.6 Å and most of the interactions are attributed to the Mg–O (2.14 Å) and Mg–Mg (3.04, 5.19, and 6.30 Å) (Fig. 4g) [46,47]. This clearly indicates that the Si atoms are homogeneously dispersed around the surface of MgO nanoplates. Interestingly, for cs-Si/Mg-0.08 and 0.45 samples, two additional peaks were observed at r = 3.65 and 4.71 Å, suggesting the Mg–Si distances are similar to the geometry of forsterite (Mg₂SiO₄) (Fig. 4g). For cs-Si/Mg-0.45 sample, we could also observe the corresponding peaks related to the core-MgO structure (around 2.1 and 3.0 Å) and to the interface magnesium silicates (around 3.2 and 4.4 Å). This indicates that the Si subunits strongly interact with the MgO surface at the interface of the core–shell structure forming magnesium silicates. Meanwhile, albeit its decreased intensity compared to the pristine SiO₂, there is a peak observed related to Mg–Si (3.62 Å), which is also observed the Mg dispersed on SiO₂ domain (Mg on SiO₂) (Fig. S7) [28]. This phase was identified for ethylene formation since the surface Mg can act as a Lewis acid sites, which is responsible for ethylene production (vide infra) [28]. Moreover, the Si–O interaction was observed for cs-Si/Mg-0.45 sample (r = 1.66 Å), which indicates the SiO₂-shell formation as core–shell

structure (Fig. 3h,n). Based on the PDF analysis, we expect that the observed 2θ shifts in PXRD is related to the local coordination of the Si subunits. For example, with the increased amount of Si, the formation of amorphous SiO₂-shell (Si–Si, ~3.0 Å) can lead the Si–O bond length longer, compared to the magnesium silicates on MgO (Mg–Si, ~3.5 Å) (Fig. 4c).

3.3. Chemical composition of the catalyst surface

To gain insights of the surface chemical composition and chemical nature of the calcined core–shell structured MgO–SiO₂ catalysts, X-ray photoelectron spectroscopy (XPS) was performed (Figs. 5a–e and S8). The characteristic peaks corresponding to Mg 2p (49 eV), Mg 2s (88 eV), Si 2p (103 eV), Si 2s (154 eV), Mg KLL auger (306 and 350 eV), O 1s (532 eV), and O KLL auger (980 eV) are present in the wide range XPS spectra of the prepared catalysts (Figs. 5a and S8). With the increased Si content, the Si/Mg ratio of the surface composition abruptly increased compared to the bulk Si/Mg ratio (Fig. 5b), showing the core-MgO particles are coated with the different SiO₂ shell thickness (Fig. 3).

Mg 2p XPS spectra showed that the pristine MgO exhibited a band centered at 49.1 eV, while the shifts to higher binding energy were observed for the core–shell structured catalysts ($\Delta_{BE,max} = 1.3$ eV) (Fig. 5c). On the contrary, compared to the pristine SiO₂ (103.2 eV), the shifts of Si 2p spectra to lower binding energy were observed for the core–shell catalysts ($\Delta_{BE,max} = 1.1$ eV), due to the incorporation of Si into the MgO domain (Fig. 5d) [45,48,49]. The above binding energy shifts clearly indicate the formation of new type of Mg and Si species for the core–shell structured catalysts, attributed to the formation of Mg–O–Si linkages. O 1s XPS spectra of SiO₂ presented a peak centered at 532.6 attributed to Si–O bond (Fig. 5e). In the case of MgO, two types of oxygen species were observed at 531.3 and 529.3 eV, attributed to the oxygen in Mg(OH)₂ and/or MgCO₃, and the one in MgO, respectively [50,51]. We could also observe shifts to lower binding energy in the O 1s spectra, which evidences the formation Mg–O–Si. The electronegativity of Si is higher than Mg (1.8 and 1.2, respectively) and the surface decoration of Si subunits on MgO can lead to the increase in binding energy of O 1s, as result of the decreased outer electron density of oxygen [52–55].

Solid-state nuclear magnetic resonance spectroscopy has been used to characterize the magnesium silicates formed during wet-kneading [20,22,44,56–68]. Fig. 5f shows ¹H–²⁹Si cross-polarization (CP) magic angle spinning (MAS) NMR spectra of the prepared catalysts. For the core–shell structured catalysts, three ²⁹Si resonances at –77, –83, and –93 ppm, attributed to the magnesium silicates formed on MgO, which can be assigned as Q¹(3Mg,1Si), Q²(2Mg,2Si) and lizardite-type Q³(1Mg,3Si) [28]. As observed by PDF analysis (Fig. 4g), the chemical environment of Mg–O–Si of core–shell MgO–SiO₂ samples is structurally similar to forsterite and enstatite (intermediate species between forsterite and enstatite [56,69]). With the higher Si content, additional ²⁹Si resonances were observed at –91, –100, and –110 ppm (Q², Q³ and Q⁴ Si species, respectively) [57,61–63,65,66], indicating the formation of SiO₂-shell.

3.4. Catalytic performance of core–shell structured MgO–SiO₂ catalysts

The pristine MgO, SiO₂, and their physical mixture catalysts have been reported for their insignificant catalytic performances for one-step ethanol-to-butadiene process [17,20,22]. We could also confirm that the MgO and SiO₂ are not active for butadiene production (Fig. 6a, Fig. S9). This clearly suggests that the pristine catalysts cannot provide the appropriate catalytic sites for the multiple steps required for ethanol-to-butadiene process, that is, the cooperation of acidic and basic sites [12,17–22,24,28,70]. As a comparison, we prepared a conventional silica–magnesia catalyst after 4 h of wet-kneading (WK-4 h, Si/Mg = 1.0), which showed the highest butadiene yield in the series of catalysts of the different Si/Mg ratio (Table S1) [20]. During the conventional

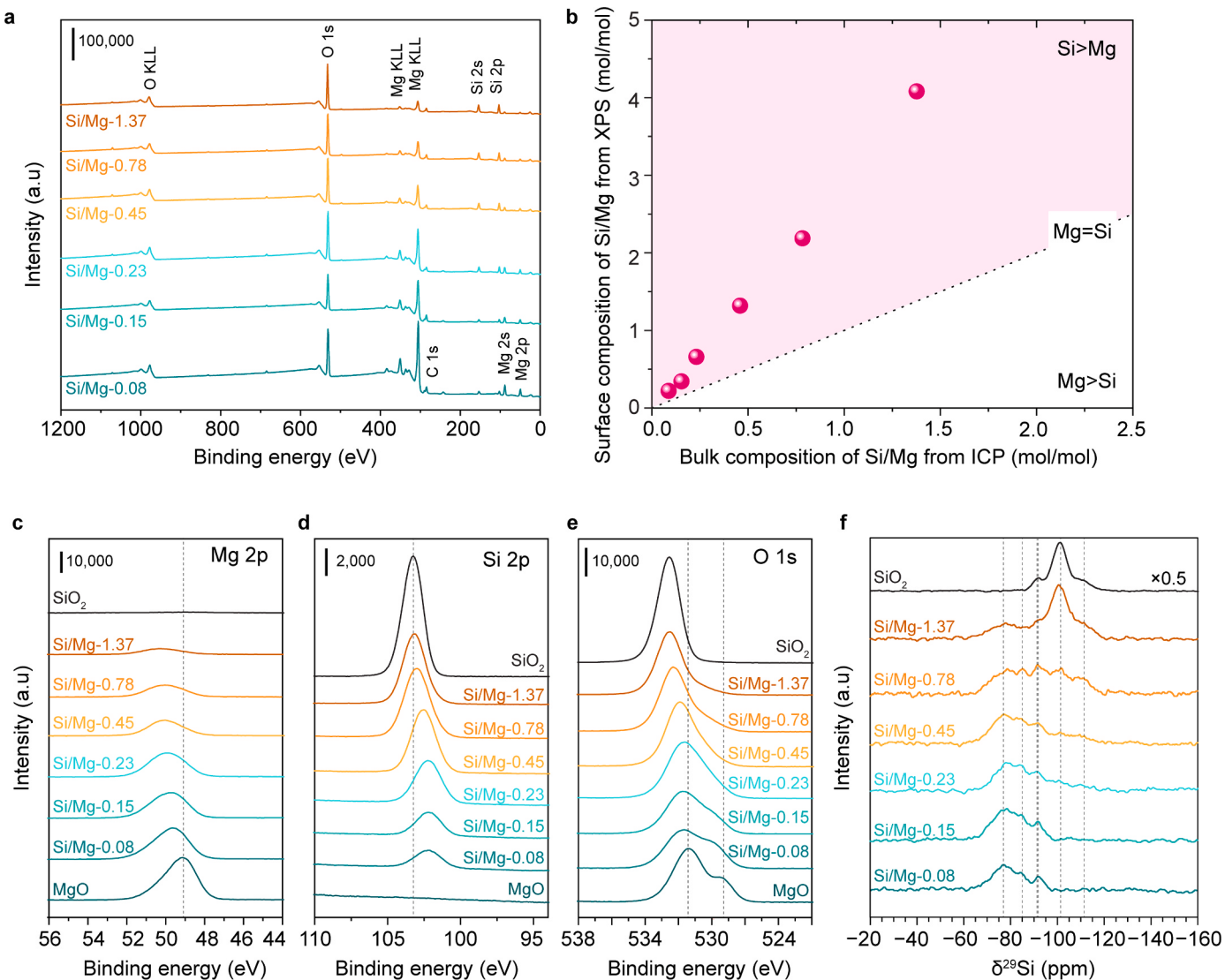


Fig. 5. X-ray photoelectron spectroscopy (XPS) and solid-state nuclear magnetic resonance (NMR) spectroscopy results for the calcined core–shell structured MgO–SiO₂ samples. (a) XPS wide scan results of the catalysts. (b) Surface composition (Si/Mg ratio) as a function of bulk composition via XPS and ICP-OES analysis. XPS narrow scans for Mg 2p (c), Si 2p (d) and O 1s (e). (f) ¹H–²⁹Si cross-polarization (CP) magic angle spinning (MAS) NMR spectra of the catalysts.

wet-kneading, the active sites (magnesium silicates) for ethanol-to-butadiene process can be formed via dissolution and cross-deposition of Si and Mg subunits on the surfaces of MgO and SiO₂, respectively [17,20,22]. The TEM-EDX analysis on WK-4 h showed that MgO and SiO₂ are in well-mixed phase and Si species were found on MgO particles (Fig. S10), that is, the active magnesium silicates for Lebedev process [20]. The conventional WK-4 h catalyst showed ~25 times higher butadiene yield compared to the pristine MgO ($Y_{BD} = 0.16\%$ and 3.8% for MgO and WK-4 h at 400°C , respectively), showing the importance of the magnesium silicates on the butadiene formation from ethanol.

Compared to the conventional WK-4 h catalyst, albeit its low Si content, the core–shell structured MgO–SiO₂ catalyst (cs-Si/Mg-0.08) exhibited ~3 times higher ethanol conversion with the drastically enhanced acetaldehyde formation (Fig. 6a, Table S1). The dehydrogenation of ethanol to acetaldehyde is considered to be catalyzed via heterolytic elimination of hydrogen from ethanol [17,28], which can be enhanced by the synergy between acid and basic sites of the SiO₂–MgO based catalysts [12,17–22,24,28,70]. For example, the dehydrogenation of ethanol is known to be influenced by the strength of basic sites of the catalysts [17,71]. Angelici *et al.* reported that, over the strong basic sites

of the SiO₂–MgO catalyst, the dehydration of ethanol is preferred rather than the dehydrogenation of ethanol [17]. For the core–shell structured MgO–SiO₂ catalysts, we observed the complete changes in the chemistry of basic sites, that is, the formation of new weak and medium strength basic sites with the disappearance of the strong basic sites related to the pristine MgO (Fig. 6i, S11,S12). Meanwhile, we observed that the number of acid sites increased by 15 times after the decoration of the Si subunits on the surface of MgO (0.002 and $0.030 \text{ mmolNH}_3 \text{ g}^{-1}$ for the pristine MgO and cs-Si/Mg-0.08, respectively) (Fig. 6i). Accordingly, we expect that the formation of the surface magnesium silicates on MgO can result in the complete alteration of acidic/basic characteristics of the catalysts, such as not only the proper balance [17], but also the close proximity between the acidic and basic sites [28].

We then tested the catalytic activity of the prepared core–shell structured MgO–SiO₂ catalysts with different Si/Mg ratios for the Lebedev process, varying the reaction temperatures from 325 to 500°C (Fig. 6b–h). We observed that the increase of the reaction temperature can lead to not only the improved ethanol conversion, but also the higher butadiene selectivity. Banu *et al.* suggested that the practical Lebedev process is operated in the kinetic regime rather than being controlled by thermodynamics [7]. We also observed that the experimental

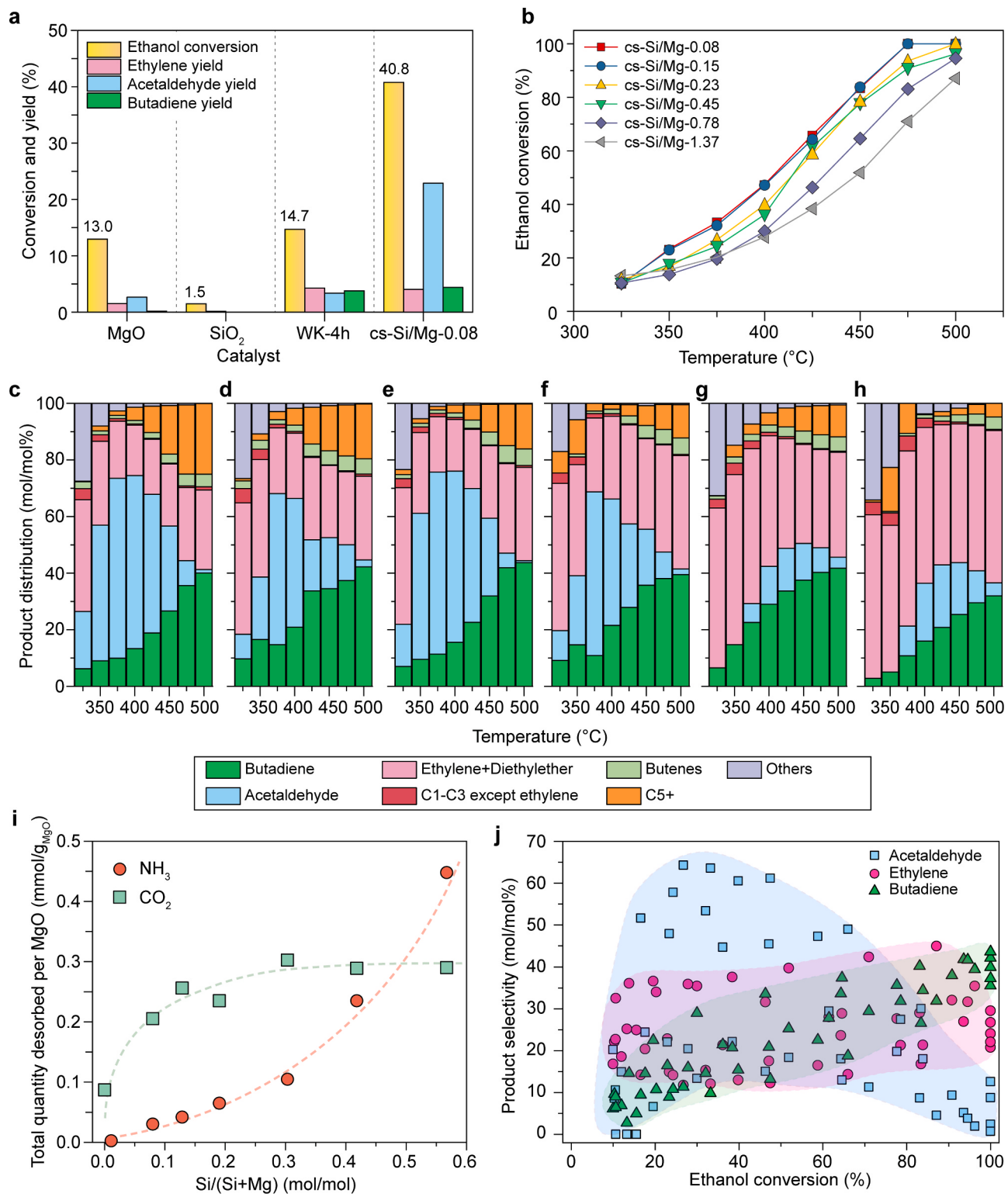


Fig. 6. Catalytic activity of the prepared catalysts. (a) The catalytic performance of pristine MgO and SiO₂, the conventional wet-kneaded silica–magnesia (WK-4 h) and the core-shell structured cs-Si/Mg-0.08 catalyst at 400 °C (WHSV 2.0 h⁻¹). (b) The ethanol conversion at different temperatures from 325 to 500 °C (WHSV 0.9 h⁻¹). (c–h) Product distribution (in mol/mol%) corresponds to the results in (b), cs-Si/Mg-0.08 (c), cs-Si/Mg-0.15 (d), cs-Si/Mg-0.23 (e), cs-Si/Mg-0.45 (f), cs-Si/Mg-0.78 (g), cs-Si/Mg-1.37 (h). (i) The number of acidic and basic sites of the prepared catalysts measured by NH₃- and CO₂-TPD. The dotted lines are added to guide the observed trend. (j) Product selectivity (acetaldehyde, ethylene and butadiene) as a function of ethanol conversion. The color shadings in (j) are added to guide the observed trend. The catalytic performances of the prepared catalysts were evaluated at 2.2 vol% ethanol feed in helium.

butadiene selectivity is much higher than secondary products such as butenes (Fig. 6c–h), although the equilibrium concentration of butadiene is much less than butenes (at 500 °C, 56% and 9% for butenes and butadiene, respectively) (Fig. S13, Table S2). Moreover, the experimental butene selectivity increased at higher reaction temperatures, whereas the butenes become thermodynamically unfavorable (Fig. S13, Table S2). Therefore, we tentatively suggest that the practical Lebedev process is not governed by thermodynamics and that the ethanol conversion and the product selectivity are mainly dependent on the catalytic activity of the catalysts [3,7].

For the low Si/Mg catalysts (Si/Mg = 0.08–0.23), most of ethanol was converted to acetaldehyde at low reaction temperatures (<400 °C), while the butadiene formation is more favorable with the consumption of acetaldehyde at higher reaction temperatures (>425 °C) (Fig. 6c–e). Da Ros *et al.* suggested that the rate-limiting step of the Lebedev process depends on the reaction temperature, such as aldol condensation and ethanol dehydrogenation is responsible as the slowest reaction step for below and above 400 °C, respectively [72]. We could also observe that the formation of heavy oxygenate compounds (C5+) at high temperatures, especially over low Si/Mg ratio catalysts (Fig. 6c–h). These

compounds can be formed on the basic sites by aldol condensation [73, 74], which also indicates the favored aldol condensation at high reaction temperature above 400 °C.

The increase of Si/Mg ratio of the core–shell structured catalysts resulted in the decrease of the ethanol conversion (Fig. 6b). This suggests that, as observed for the pristine SiO₂ (Fig. 6a), the excessive SiO₂ shell of the core–shell structured catalysts is not active for the ethanol conversion. Interestingly, it can be noted that the butadiene selectivity for the high Si/Mg catalysts (Si/Mg = 0.45–1.37) is comparable to the low Si/Mg catalysts (Fig. 6b–h). This result clearly reveals that the inherently formed magnesium silicates (Mg–O–Si), which are located at the interface between core-MgO and shell-SiO₂, provided the catalytic active sites required to ethanol-to-butadiene pathway. Meanwhile, the ethylene selectivity increased with the higher Si/Mg ratio of the core–shell structured MgO–SiO₂ catalysts (Fig. 6g,h). For cs-Si/Mg-1.37, the ethylene selectivity is higher than 50% with the unfavorable formation of acetaldehyde, indicating that the competitive reaction between dehydration and dehydrogenation of ethanol to ethylene and acetaldehyde, respectively [22]. We expect the increased ethylene selectivity for the catalysts with higher Si/Mg ratio is attributed to the off-balance

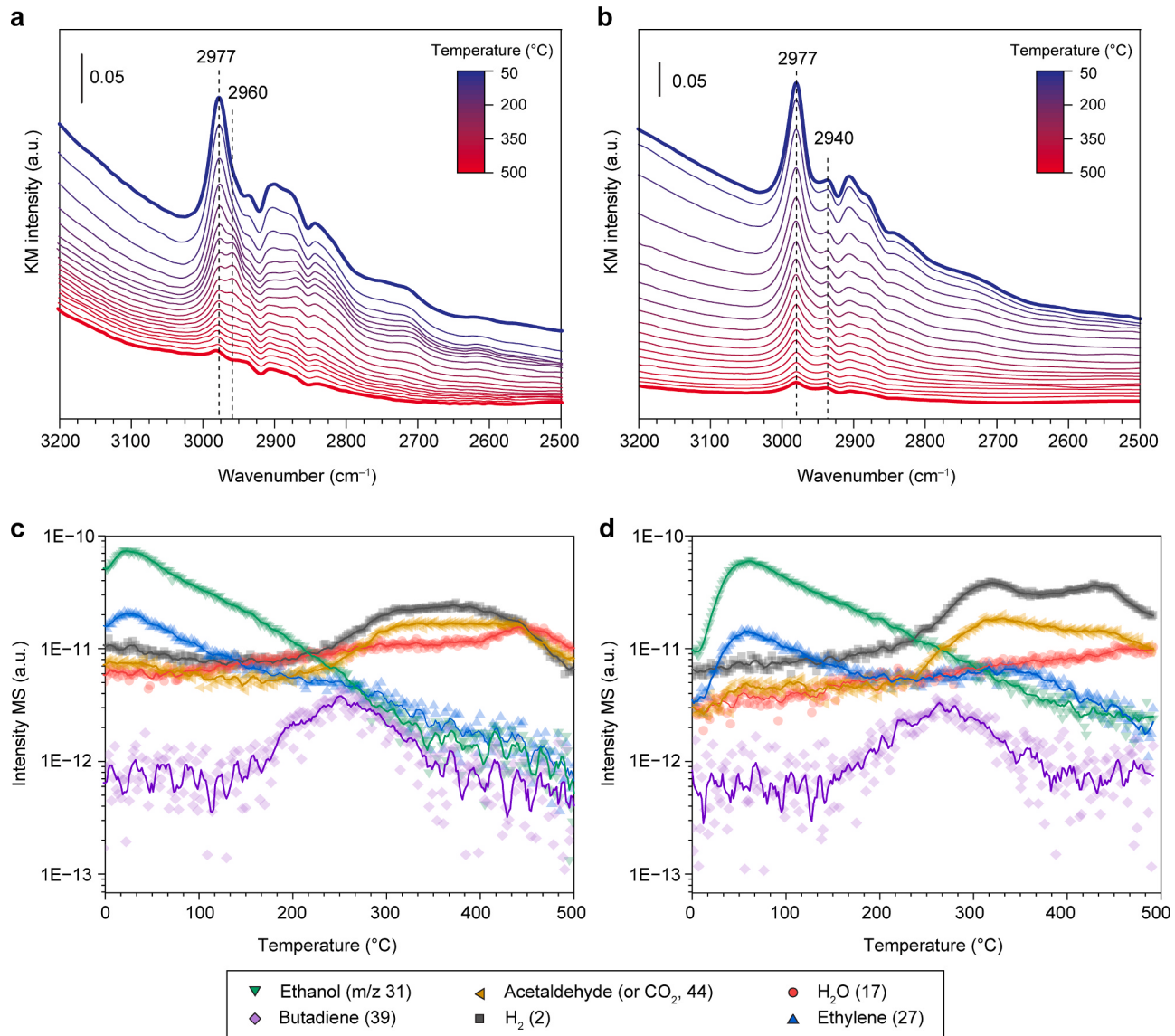


Fig. 7. *Operando* diffuse reflectance infrared fourier transform spectroscopy combined with online mass spectrometry (DRIFTS-MS) results. (a,c) The conventional wet-kneaded SiO₂-MgO catalyst after 4 h of wet-kneading (WK-4 h) and (b,d) the core–shell structured MgO–SiO₂ (cs-Si/Mg-0.45). The spectra were acquired during temperature programmed surface reaction (TPSR) for chemisorbed ethanol species on the catalysts with the temperature range between 50 to 500 °C.

between the acidic and basic sites. For example, we could observe the drastic increase of the number of acid sites, while the number of basic sites are saturated with the increase of Si/Mg ratio (Fig. 6i, Fig. S11, S12). As the pristine SiO_2 has negligible amount of acidic sites, this indicates the formation of the Si-rich magnesium silicate phase for the catalysts higher Si/Mg ratios (Figs. 4 and S7), which is responsible for the dehydration of ethanol to ethylene production (Fig. 6g,h) [28]. Fig. 6j shows the relationships between ethanol conversion and product selectivity. Albeit its rather scattered distribution of experimental results, we expect that it shows the importance of the cooperation of the catalytic properties and the process parameters (e.g., reaction temperature) on the one-step ethanol-to-butadiene process. Ethylene is known to be formed by a side reaction (direct dehydration of ethanol), competing with acetaldehyde on the limited number of catalytic sites [75]. Meanwhile, as the ethanol conversion increases, the acetaldehyde selectivity followed volcano-shaped dependence, while butadiene selectivity continuously increases, suggesting that acetaldehyde is an intermediate for the ethanol-to-butadiene reaction [8].

3.5. Mechanistic investigation using operando DRIFTS–MS spectroscopy

The mechanism of ethanol-to-butadiene on the core–shell structured MgO–SiO_2 catalysts was investigated using *operando* diffuse reflectance infrared Fourier transform spectroscopy coupled with mass spectrometry (DRIFTS–MS) using temperature programmed surface reaction technique (TPSR) (Fig. 7). The DRIFTS–MS results of the core–shell catalyst (cs-Si/Mg-0.45) were compared to the conventional wet-kneaded silica-magnesia (WK-4 h). It should be noted that the WK-4 h is composed of two heterogenous catalyst particles and surfaces (Si/MgO and Mg/SiO_2), due to the simultaneous dissolution and cross-deposition of Si and Mg subunits on Mg(OH)_2 and SiO_2 , respectively [28]. For both samples (WK-4 h and cs-Si/Mg-0.45), the adsorbed ethanol on the catalyst surfaces showed the asymmetric CH stretching from the CH_3 group at 2977 cm^{-1} at low temperature [76,77]. During the surface reaction at 175°C , a new band at 2960 cm^{-1} was observed for WK-4 h sample, attributed to another type of asymmetric stretching of CH_3 in chemisorbed ethanol [78]. This indicates the surface heterogeneity of the conventional wet-kneaded catalyst (WK-4 h), which can lead to the different adsorption modes of ethanol. According to the mechanism for dehydration of ethanol [79,80], the E1-type reaction occurs to remove β -hydrogen from the adsorbed ethanol species, yielding ethylene.

Meanwhile, compared to the conventional WK-4 h, all of the CH vibrations decreased monotonically with temperature for cs-Si/Mg-0.45 catalyst, clearly suggesting that more uniform adsorption sites for ethanol are provided by the core–shell structured MgO–SiO_2 catalyst. Notably, an additional IR band is observed at $\sim 2940 \text{ cm}^{-1}$, which is attributed to the asymmetric CH stretching of the CH_2 group at the alpha carbon of adsorbed ethanol [13,70,78]. Based on E1cB-type reaction mechanism, the removal of α -hydrogen is important for the dehydrogenation of ethanol to acetaldehyde, including heterolytic elimination of H_2 [17,79–83]. It can be also noted that the surface hydroxyl groups of the core–shell structured MgO–SiO_2 catalysts can interact with ethanol, showing a broad OH stretching band in the $3600\text{--}3200 \text{ cm}^{-1}$ region (Fig. S14). This indicates the intermolecular hydrogen bonding of ethanol with the catalyst surface [28,84], which can promote the heterolytic elimination of hydrogen from ethanol and consequently, acetaldehyde is preferably produced for the core–shell catalyst (Fig. 6) [17, 28,79,81–87].

Interestingly, we observed that the formation of butadiene is maximized at $\sim 260^\circ\text{C}$ and decreased, although there are considerable amount of acetaldehyde at higher reaction temperatures (Fig. 7c,d). This suggests that a Meerwein–Ponndorf–Verley–Oppenauer-type reaction is involved for ethanol-to-butadiene process [8]. In other words, the adjacent ethanol–intermediates can react to form butadiene (reduction of crotonaldehyde by ethanol). Meanwhile, the strong adsorption of

formed acetaldehyde on the catalyst surface was not observed (absence of IR bands of acetaldehyde at 3020 and 2793 cm^{-1} (CH_3 and CH stretching, respectively, [13,28,70]), which were predominantly observed for the pristine MgO surface [28]). In this regard, we propose that the core–shell structured MgO–SiO_2 catalysts could reduce the affinity of the intermediates on the catalyst surface and enable the subsequent reactions to butadiene such as aldol condensation, dehydrations of acetaldol and crotyl alcohol, by the cooperative interplay of acidic Si species on basic MgO . Thus, to obtain proper balance in acidic and basic sites of $\text{SiO}_2\text{-MgO}$ catalysts [3,8,17,20–22,26,70,88,89], not only the location, but also the local structure with the Si/Mg ratio must be considered for the selective butadiene production in the Levedev process.

4. Conclusions

In summary, we demonstrated a group of core–shell structured MgO–SiO_2 as second generation of Lebedev catalysts, where the Si subunits were selectively deposited on the MgO nanoparticles as surface magnesium silicates. Compared to the conventional wet-kneaded silica-magnesia catalyst system, the core–shell structured MgO–SiO_2 catalysts can be prepared with ~ 40 times less amount of Si source, while achieving ~ 3 times higher ethanol conversion. With the inherent structural advantages of the core–shell structured MgO–SiO_2 catalysts, the cooperative interplay between the acidic and basic sites could promote the formation of acetaldehyde, a key reaction intermediate in the Lebedev process. Based on the insights provided in this study, we believe further researches on the second generation Lebedev catalysts such as the use of dehydrogenation promoters can lead to boosted butadiene selectivity.

CRediT authorship contribution statement

Sang-Ho Chung: Conceptualization, Validation, Data curation, Formal analysis, Investigation, Writing – original draft, Writing – review & editing; **Juan Carlos Navarro de Miguel:** Data curation, Formal analysis, Investigation, Writing – review & editing; **Teng Li:** Visualization, Investigation, Formal analysis, Validation; **Polina Lavrik:** Visualization, Investigation, Formal analysis, Validation; **Daria Poloneeva:** Visualization, Investigation, Formal analysis, Validation; **Sarah Komaty:** Visualization, Investigation, Formal analysis, Validation; **Mohamed Nejib Hedhili:** Visualization, Investigation, Formal analysis; **Youyou Yuan:** Visualization, Investigation, Formal analysis; **Wajed H. Anbari:** Visualization, Investigation, Formal analysis; **Moussa Zaarour:** Visualization, Investigation, Formal analysis; **Cristina Martin:** Visualization, Investigation, Formal analysis; **Tuiana Shoinkhorova:** Visualization, Investigation, Formal analysis; **Edy Abou-Hamad:** Visualization, Investigation, Formal analysis; **Jorge Gascon:** Supervision, Writing – review & editing, Investigation; **Javier Ruiz-Martinez:** Conceptualization, Supervision, Writing – original draft, Writing – review & editing, Funding acquisition, Investigation.

Declaration of Competing Interest

The authors declare the following financial interests/personal relationships which may be considered as potential competing interests: Javier Ruiz-Martinez has patent #63/528,997 pending to King Abdullah University of Science and Technology.

Data availability

Data will be made available on request.

Acknowledgements

The authors are grateful for the funding support from King Abdullah

University of Science and Technology, baseline grant BAS/1/1402-01-01. We thank Eganathan Kaliyamoorthy for ICP-OES, Xinqi Tang and Dr. Chris Canlas for technical support for solid-state NMR spectroscopy.

Data availability

Data will be made available on request.

Appendix A. Supporting information

Supplementary data associated with this article can be found in the online version at doi:10.1016/j.apcatb.2023.123628.

Appendix A. Supporting information

Supplementary data associated with this article can be found in the online version at doi:10.1016/j.apcatb.2023.123628.

References

- [1] P.C. Bruijnincx, B.M. Weckhuysen, Shale gas revolution: an opportunity for the production of biobased chemicals?, *Angew. Chem. Int. Ed. Engl.* 52 (2013) 11980–11987.
- [2] C. Angelici, B.M. Weckhuysen, P.C. Bruijnincx, Chemocatalytic conversion of ethanol into butadiene and other bulk chemicals, *ChemSusChem* 6 (2013) 1595–1614.
- [3] E.V. Makshina, M. Dusselier, W. Janssens, J. Degreve, P.A. Jacobs, B.F. Sels, Review of old chemistry and new catalytic advances in the on-purpose synthesis of butadiene, *Chem. Soc. Rev.* 43 (2014) 7917–7953.
- [4] D. Cespi, F. Passarini, I. Vassura, F. Cavani, Butadiene from biomass, a life cycle perspective to address sustainability in the chemical industry, *Green. Chem.* 18 (2016) 1625–1638.
- [5] N. Miyake, G. Brezicki, R.J. Davis, Cascade Reaction of Ethanol to Butadiene over Multifunctional Silica-Supported Ag and ZrO₂ Catalysts, *ACS Sustain. Chem. Eng.* 10 (2022) 1020–1035.
- [6] J.Y. Zhang, E. Yoo, B.H. Davison, D.X. Liu, J.A. Schaidle, L. Tao, Z.L. Li, Towards cost-competitive middle distillate fuels from ethanol within a market-flexible biorefinery concept, *Green. Chem.* 23 (2021) 9534–9548.
- [7] I. Banu, A.V. Brosteau, G. Bumbac, G. Bozga, Ethanol conversion to butadiene: a thermodynamic analysis, *Ind. Eng. Chem. Res.* 60 (2021) 13071–13083.
- [8] G. Pomalaž, P.A. Ponton, M. Capron, F. Dumeignil, Ethanol-to-butadiene: the reaction and its catalysts, *Catal. Sci. Technol.* 10 (2020) 4860–4911.
- [9] I. Bin Samudin, H. Zhang, S. Jaenicke, G.K. Chuah, Recent Advances in Catalysts for the Conversion of Ethanol to Butadiene, *Chem. Asian J.* 15 (2020) 4199–4214.
- [10] J. Ostromislenskiy, Production of butadiene, *J. Russ. Phys. Chem. Soc.* 47 (1915) 1472–1506.
- [11] G.M. Cabello González, A.L. Villanueva Perales, A. Martínez, M. Campoy, F. Vidal-Barrero, Conversion of aqueous ethanol/acetaldehyde mixtures into 1,3-butadiene over a mesostructured Ta-SBA-15 catalyst: Effect of reaction conditions and kinetic modelling, *Fuel Process. Technol.* 226 (2022), 107092–107092.
- [12] D. Dussol, N. Cadran, N. Laloue, L. Renaudot, J.M. Schweitzer, New insights of butadiene production from ethanol: Elucidation of concurrent reaction pathways and kinetic study, *Chem. Eng. J.* 391 (2020), 123586–123586.
- [13] A. Chieregato, J. Velasquez Ochoa, C. Bandinelli, G. Fornasari, F. Cavani, M. Mella, On the chemistry of ethanol on basic oxides: revising mechanisms and intermediates in the Lebedev and Guerbet reactions, *ChemSusChem* 8 (2015) 377–388.
- [14] V.L. Sushkevich, I.I. Ivanova, Mechanistic study of ethanol conversion into butadiene over silver promoted zirconia catalysts, *Appl. Catal. B-Environ.* 215 (2017) 36–49.
- [15] V. Gruber, A. Sun, J.J. Fripiat, Catalytic Properties of Aluminated Sepiolite in Ethanol Conversion, *Catal. Lett.* 34 (1995) 359–364.
- [16] A. Boje, W.E. Taifan, H. Strom, T. Bucko, J. Baltrusaitis, A. Hellman, First-principles-informed energy span and microkinetic analysis of ethanol catalytic conversion to 1,3-butadiene on MgO, *Catal. Sci. Technol.* 11 (2021) 6682–6694.
- [17] C. Angelici, M.E.Z. Velthoen, B.M. Weckhuysen, P.C.A. Bruijnincx, Influence of acid-base properties on the Lebedev ethanol-to-butadiene process catalyzed by SiO₂-MgO materials, *Catal. Sci. Technol.* 5 (2015) 2869–2879.
- [18] G. Natta, R. Rigamonti, Studio roentgenografico chimico dei catalizzatori usati per la produzione del butadiene dall'alcool, *Chim. Ind.* 29 (1947) 239–243.
- [19] S. Kvisle, A. Aguero, R.P.A. Sneeden, Transformation of Ethanol into 1,3-Butadiene over Magnesium-Oxide Silica Catalysts, *Appl. Catal.* 43 (1988) 117–131.
- [20] S.-H. Chung, C. Angelici, S.O.M. Hinterding, M. Weingarth, M. Baldus, K. Houben, B.M. Weckhuysen, P.C.A. Bruijnincx, Role of Magnesium Silicates in Wet-Kneaded Silica-Magnesia Catalysts for the Lebedev Ethanol-to-Butadiene Process, *ACS Catal.* 6 (2016) 4034–4045.
- [21] C. Angelici, M.E. Velthoen, B.M. Weckhuysen, P.C. Bruijnincx, Effect of preparation method and CuO promotion in the conversion of ethanol into 1,3-butadiene over SiO₂-MgO catalysts, *ChemSusChem* 7 (2014) 2505–2515.
- [22] S.H. Chung, A. Ramirez, T. Shoinkhorova, I. Mukhametov, E. Abou-Hamad, S. Telalovic, J. Gascon, J. Ruiz-Martinez, The Importance of Thermal Treatment on Wet-Kneaded Silica-Magnesia Catalyst and Lebedev Ethanol-to-Butadiene Process, *Nanometer. (Basel)* 11 (2021), 579–579.
- [23] M. Lewandowski, G.S. Babu, M. Vezzoli, M.D. Jones, R.E. Owen, D. Mattia, P. Plucinski, E. Mikolajski, A. Ochenduszko, D.C. Apperley, Investigations into the conversion of ethanol to 1,3-butadiene using MgO:SiO₂ supported catalysts, *Catal. Commun.* 49 (2014) 25–28.
- [24] W.E. Taifan, T. Bucko, J. Baltrusaitis, Catalytic conversion of ethanol to 1,3-butadiene on MgO: A comprehensive mechanism elucidation using DFT calculations, *J. Catal.* 346 (2017) 78–91.
- [25] G.M. Cabello González, P. Concepción, A.L. Villanueva Perales, A. Martínez, M. Campoy, F. Vidal-Barrero, Ethanol conversion into 1,3-butadiene over a mixed Hf-Zn catalyst: Effect of reaction conditions and water content in ethanol, *Fuel Process. Technol.* 193 (2019) 263–272.
- [26] W. Janssens, E.V. Makshina, P. Vanelderken, F. De Clippele, K. Houthoofd, S. Kerkhofs, J.A. Martens, P.A. Jacobs, B.F. Sels, Ternary Ag/MgO-SiO₂ catalysts for the conversion of ethanol into butadiene, *ChemSusChem* 8 (2015) 913.
- [27] X.X. Huang, Y. Men, J.G. Wang, W. An, Y.Q. Wang, Highly active and selective binary MgO-SiO₂ catalysts for the production of 1,3-butadiene from ethanol, *Catal. Sci. Technol.* 7 (2017) 168–180.
- [28] S.-H. Chung, T. Li, T. Shoinkhorova, S. Komaty, A. Ramirez, I. Mukhametov, E. Abou-Hamad, G. Shterk, S. Telalovic, A. Dikhtarenko, B. Sirks, P. Lavrik, X. Tang, B.M. Weckhuysen, P.C.A. Bruijnincx, J. Gascon, J. Ruiz-Martinez, Origin of active sites on silica-magnesia catalysts and control of reactive environment in the one-step ethanol-to-butadiene process, *Nat. Catal.* 6 (2023) 363–376.
- [29] D. Niu, Z. Ma, Y. Li, J. Shi, Synthesis of core-shell structured dual-mesoporous silica spheres with tunable pore size and controllable shell thickness, *J. Am. Chem. Soc.* 132 (2010) 15144–15147.
- [30] J. Goworek, A. Kierys, W. Gac, A. Borowka, R. Kusak, Thermal Degradation of Ctab in as-Synthesized Mcm-41, *J. Therm. Anal. Calorim.* 96 (2009) 375–382.
- [31] D. Nied, K. Enemark-Rasmussen, E. L'Hopital, J. Skibsted, B. Lothenbach, Properties of magnesium silicate hydrates (M-S-H), *Cem. Concr. Res.* 79 (2016) 323–332.
- [32] E. Bernard, B. Lothenbach, D. Rentsch, I. Pochard, A. Dauzeres, Formation of magnesium silicate hydrates (M-S-H), *Phys. Chem. Earth* 99 (2017) 142–157.
- [33] X.Z. Guo, T. Yoshino, S.B. Chen, X. Wu, J.F. Zhang, Partial dehydration of brucite and its implications for water distribution in the subducting oceanic slab, *Geosci. Front.* 13 (2022), 101342–101342.
- [34] N. An, Y. Wang, M. Li, H. Lin, F. Qu, The synthesis of core-shell Cu95S@mSiO₂-ICG@PEG-LA for photothermal and photodynamic therapy, *N. J. Chem.* 42 (2018) 18318–18327.
- [35] R. Soltani, A. Marjani, R. Soltani, S. Shirazian, Hierarchical multi-shell hollow micro-meso-macroporous silica for Cr(VI) adsorption, *Sci. Rep.* 10 (2020) 9788.
- [36] M. Waseem, S. Mustafa, A. Naeem, K.H. Shah, I. Shah, Mechanism of Cd (II) sorption on silica synthesized by sol-gel method, *Chem. Eng. J.* 169 (2011) 78–83.
- [37] J. Chen, R. Zhang, L. Han, B. Tu, D. Zhao, One-pot synthesis of thermally stable gold@mesoporous silica core-shell nanospheres with catalytic activity, *Nano Res.* 6 (2013) 871–879.
- [38] E. Goria, L. Duarte-Correia, N. Bashiri, W. Hetaba, R. Schomaeker, A. Thomas, Rational design of tandem catalysts using a core-shell structure approach, *Nanoscale Adv.* 3 (2021) 3454–3459.
- [39] D.A. Kurdyukov, D.A. Eurov, D.A. Kirilenko, V.V. Sokolov, V.G. Golubev, Tailoring the size and microporosity of Stöber silica particles, *Microporous Mesoporous Mater.* 258 (2018) 205–210.
- [40] X. Jiang, H. Zhang, M. Yue, S. Zhang, Y. Li, W. Xu, Synthesis of organic hybrid super-microporous silicas as an adsorbent for dyes removal from water, *Microporous Mesoporous Mater.* 288 (2019), 109598.
- [41] E.Y. Stoyviaga, D.A. Eurov, D.A. Kurdyukov, N.V. Glebova, D.A. Kirilenko, M. V. Tomkovich, V.G. Golubev, Formation of spherical microporous silica particles from organosilane and quat molecules, *Colloids Surf. A: Physicochem. Eng. Asp.* 650 (2022), 129633.
- [42] S.K. Shah, S.K. Chatterjee, A. Bhattacharai, Micellization of cationic surfactants in alcohol — water mixed solvent media, *J. Mol. Liq.* 222 (2016) 906–914.
- [43] S. Shylesh, A.A. Gokhale, C.D. Scown, D. Kim, C.R. Ho, A.T. Bell, From Sugars to Wheels: The Conversion of Ethanol to 1,3-Butadiene over Metal-Promoted Magnesia-Silicate Catalysts, *ChemSusChem* 9 (2016) 1462–1472.
- [44] J. Temuujin, K. Okada, K.J.D. MacKenzie, Role of water in the mechanochemical reactions of MgO-SiO₂ systems, *J. Solid State Chem.* 138 (1998) 169–177.
- [45] B. Szabó, G. Novodárszki, Z. Pászti, A. Domján, J. Valyon, J. Hancsók, R. Barthos, MgO-SiO₂ catalysts for the ethanol to butadiene reaction: the effect of lewis acid promoters, *ChemCatChem* 12 (2020) 5686–5696.
- [46] E. Bernard, B. Lothenbach, C. Chlique, M. Wyrzykowski, A. Dauzeres, I. Pochard, C. Cau-Dit-Coumes, Characterization of magnesium silicate hydrate (M-S-H), *Cem. Concr. Res.* 116 (2019) 309–330.
- [47] E. Bernard, B. Lothenbach, C. Cau-Dit-Coumes, C. Chlique, A. Dauzeres, I. Pochard, Magnesium and calcium silicate hydrates, Part I: Investigation of the possible magnesium incorporation in calcium silicate hydrate (C-S-H) and of the calcium in magnesium silicate hydrate (M-S-H), *Appl. Geochem.* 89 (2018) 229–242.
- [48] Q.Q. Zhu, B. Wang, T.W. Tan, Conversion of Ethanol and Acetaldehyde to Butadiene over MgO-SiO₂ Catalysts: Effect of Reaction Parameters and Interaction between MgO and SiO₂ on Catalytic Performance, *Acs Sustain. Chem. Eng.* 5 (2017) 722–733.
- [49] R. Brambilla, G.P. Pires, J.H.Z. dos Santos, M.S.L. Miranda, B. Chornik, Octadecylsilane-modified silicas prepared by grafting and sol-gel methods, *J. Electron Spectrosc. Relat. Phenom.* 156 (2007) 413–420.
- [50] F. Khairallah, A. Glisenti, XPS Study of MgO Nanopowders Obtained by Different Preparation Procedures, *Surf. Sci. Spectra* 13 (2006) 58–71.
- [51] A. Le Febvrier, J. Jensen, P. Eklund, Wet-cleaning of MgO(001): Modification of surface chemistry and effects on thin film growth investigated by x-ray

- photoelectron spectroscopy and time-of-flight secondary ion mass spectroscopy, *J. Vac. Sci. Technol. A: Vac., Surf., Films* 35 (2017), 021407-021407.
- [52] Y. Zhang, L.L. Zhu, L.G. Chen, L.Q. Liu, G.T. Ye, Influence of Magnesia on Demoulding Strength of Colloidal Silica-Bonded Castables, *Rev. Adv. Mater. Sci.* 58 (2019) 32–37.
- [53] T.L. Barr, The Nature of the Relative Bonding Chemistry in Zeolites - an Xps Study, *Zeolites* 10 (1990) 760–765.
- [54] T.L. Barr, An Xps Study of Si as It Occurs in Adsorbents, Catalysts, and Thin-Films, *Appl. Surf. Sci.* 15 (1983) 1–35.
- [55] J.T. Klopogge, L.V. Duong, B.J. Wood, R.L. Frost, XPS study of the major minerals in bauxite: gibbsite, bayerite and (pseudo-)boehmite, *J. Colloid Interface Sci.* 296 (2006) 572–576.
- [56] K.J.D. MacKenzie, R.H. Meinhold, Thermal reactions of chrysotile revisited: a ^{29}Si and ^{25}Mg MAS NMR study, *Am. Mineral.* 79 (1994) 43–50.
- [57] K.J.D. MacKenzie, R.H. Meinhold, The thermal reactions of talc studied by ^{29}Si and ^{25}Mg MAS NMR, *Thermochim. Acta* 244 (1994) 195–203.
- [58] J.F. Stebbins, W.R. Panero, J.R. Smyth, D.J. Frost, Forsterite, wadsleyite, and ringwoodite (Mg_2SiO_4): ^{29}Si NMR constraints on structural disorder and effects of paramagnetic impurity ions, *Am. Mineral.* 94 (2009) 626–629.
- [59] J.F. Stebbins, J.R. Smyth, W.R. Panero, D.J. Frost, Forsterite, hydrous and anhydrous wadsleyite and ringwoodite (Mg_2SiO_4): ^{29}Si NMR results for chemical shift anisotropy, spin-lattice relaxation, and mechanism of hydration, *Am. Mineral.* 94 (2009) 905–915.
- [60] J.-B. d'Espinoose de la Caillerie, M. Kermarec, O. Clause, ^{29}Si NMR Observation of an Amorphous Magnesium Silicate Formed during Impregnation of Silica with Mg (II) in Aqueous Solution, *J. Phys. Chem.* 99 (2002) 17273–17281.
- [61] J. d'Espinoose de la Caillerie, V. Gruver, J. Fripiat, Modification of the surface properties of natural phyllosilicate sepiolite by secondary isomorphic substitution, *J. Catal.* (1995) 420–430.
- [62] J.S. Hartman, R.L. Millard, Gel synthesis of magnesium silicates: A ^{29}Si magic angle spinning NMR study, *Phys. Chem. Miner.* 17 (1990) 1–8.
- [63] M. Magi, E. Lippmaa, A. Samoson, G. Engelhardt, A.R. Grimmer, Solid-state high-resolution silicon- 29 chemical shifts in silicates, *J. Phys. Chem.* 88 (2002) 1518–1522.
- [64] K.D. Litasov, E. Ohtani, Effect of water on the phase relations in Earth's mantle and deep water cycle, *Advances in High-Pressure Mineralogy*, *Geol. Soc. Am.* (2007) 115–156.
- [65] E. Lippmaa, M. Maegi, A. Samoson, G. Engelhardt, A.R. Grimmer, Structural studies of silicates by solid-state high-resolution silicon- 29 NMR, *J. Am. Chem. Soc.* 102 (2002) 4889–4893.
- [66] S.A. Walling, H. Kinoshita, S.A. Bernal, N.C. Collier, J.L. Provis, Structure and properties of binder gels formed in the system $\text{Mg}(\text{OH})_2\text{-SiO}_2\text{-H}_2\text{O}$ for immobilisation of Magnox sludge, *Dalton Trans.* 44 (2015) 8126–8137.
- [67] K.J.D. MacKenzie, S. Bradley, J.V. Hanna, M.E. Smith, Magnesium analogues of aluminosilicate inorganic polymers (geopolymers) from magnesium minerals, *J. Mater. Sci.* 48 (2013) 1787–1793.
- [68] K. Chabrol, M. Gressier, N. Pebere, M.J. Menu, F. Martin, J.P. Bonino, C. Marichal, J. Brendle, Functionalization of synthetic talc-like phyllosilicates by alkoxyorganosilane grafting, *J. Mater. Chem.* 20 (2010) 9695–9706.
- [69] G. Rim, A.K. Marchese, P. Stallworth, S.G. Greenbaum, A.-H.A. Park, ^{29}Si solid state MAS NMR study on leaching behaviors and chemical stability of different Mg-silicate structures for CO_2 sequestration, *Chem. Eng. J.* 396 (2020), 125204–125204.
- [70] W.E. Taifan, G.X. Yan, J. Baltrusaitis, Surface chemistry of MgO/SiO_2 catalyst during the ethanol catalytic conversion to 1,3-butadiene: in-situ DRIFTS and DFT study, *Catal. Sci. Technol.* 7 (2017) 4648–4668.
- [71] W.E. Taifan, Y. Li, J.P. Baltrus, L. Zhang, A.I. Frenkel, J. Baltrusaitis, Operando Structure Determination of Cu and Zn on Supported MgO/SiO_2 Catalysts during Ethanol Conversion to 1,3-Butadiene, *ACS Catal.* 9 (2018) 269–285.
- [72] S. Da Ros, M.D. Jones, D. Mattia, M. Schwaab, E. Barbosa-Coutinho, R.C. Rabelo-Neto, F.B. Noronha, J.C. Pinto, Microkinetic analysis of ethanol to 1,3-butadiene reactions over MgO-SiO_2 catalysts based on characterization of experimental fluctuations, *Chem. Eng. J.* 308 (2017) 988–1000.
- [73] H. Wang, G. Miao, L. Kong, H. Luo, Y. Zhang, X. Zhao, S. Li, Y. Sun, Efficient one-pot valorization of ethanol to 1-butanol over an earth-abundant Ni-MgO catalyst under mild conditions, *Sustain. Energy Fuels* 4 (2020) 1612–1615.
- [74] J.I. Di Cosimo, C.R. a Apestegui, M.J.L. Ginés, E. Iglesia, Structural Requirements and Reaction Pathways in Condensation Reactions of Alcohols on Mg_yAlO_x Catalysts, *J. Catal.* 190 (2000) 261–275.
- [75] S.-H. Chung, A. Ramirez, T. Shokinhorova, I. Mukhametov, E. Abou-Hamad, S. Telalovic, J. Gascon, J. Ruiz-Martinez, The Importance of Thermal Treatment on Wet-Kneaded Silica–Magnesia Catalyst and Lebedev Ethanol-to-Butadiene Process, *Nanomaterials* 11 (2021) 579.
- [76] M. Singh, N. Zhou, D.K. Paul, K.J. Klabunde, IR spectral evidence of aldol condensation: Acetaldehyde adsorption over TiO_2 surface, *J. Catal.* 260 (2008) 371–379.
- [77] T. Moteki, D.W. Flaherty, Mechanistic Insight to C-C Bond Formation and Predictive Models for Cascade Reactions among Alcohols on Ca- and Sr-Hydroxyapatites, *Acs Catal.* 6 (2016) 4170–4183.
- [78] J.V. Ochoa, A. Malmusi, C. Recchi, F. Cavani, Understanding the Role of Gallium as a Promoter of Magnesium Silicate Catalysts for the Conversion of Ethanol into Butadiene, *Chemcatchem* 9 (2017) 2128–2135.
- [79] V. Díez, Acid-base properties and active site requirements for elimination reactions on alkali-promoted MgO catalysts, *Catal. Today* 63 (2000) 53–62.
- [80] Y. Shinohara, H. Satozono, T. Nakajima, S. Suzuki, S. Mishima, Study of the Interaction of Ethanol with the Bronsted and Lewis Acid Sites on Metal Oxide Surfaces Using the DV-X.ALPHA. Method, *J. Chem. Softw.* 4 (1998) 41–50.
- [81] L. Qi, Y. Zhang, M.A. Conrad, C.K. Russell, J. Miller, A.T. Bell, Ethanol Conversion to Butadiene over Isolated Zinc and Yttrium Sites Grafted onto Dealuminated Beta Zeolite, *J. Am. Chem. Soc.* 142 (2020) 14674–14687.
- [82] T. Tsuchida, J. Kubo, T. Yoshioka, S. Sakuma, T. Takeguchi, W. Ueda, Reaction of ethanol over hydroxyapatite affected by Ca/P ratio of catalyst, *J. Catal.* 259 (2008) 183–189.
- [83] J.T. Kozlowski, R.J. Davis, Heterogeneous catalysts for the guerbet coupling of alcohols, *Acs Catal.* 3 (2013) 1588–1600.
- [84] H.T. Abdulrazzaq, A. Rahmani Chokanlu, B.G. Frederick, T.J. Schwartz, Reaction kinetics analysis of ethanol dehydrogenation catalyzed by MgO-SiO_2 , *ACS Catal.* 10 (2020) 6318–6331.
- [85] J.I. Di Cosimo, V.K. Diez, M. Xu, E. Iglesia, C.R. Apéstegui, Structure and Surface and Catalytic Properties of Mg-Al Basic Oxides, *J. Catal.* 178 (1998) 499–510.
- [86] M.J.L. Gines, E. Iglesia, Bifunctional condensation reactions of alcohols on basic oxides modified by copper and potassium, *J. Catal.* 176 (1998) 155–172.
- [87] T.W. Birk, J.T. Kozlowski, R.J. Davis, Isotopic transient analysis of the ethanol coupling reaction over magnesia, *J. Catal.* 298 (2013) 130–137.
- [88] G. Pomalaza, M. Capron, V. Ordomsky, F. Dumeignil, Recent Breakthroughs in the Conversion of Ethanol to Butadiene, *Catalysts* 6 (2016), 203–203.
- [89] W.E. Taifan, J. Baltrusaitis, In situ spectroscopic insights on the molecular structure of the MgO/SiO_2 catalytic active sites during ethanol conversion to 1,3-butadiene, *J. Phys. Chem. C* 122 (2018) 20894–20906.